Arabian Journal for Science and Engineering (2022) 47:15303–15321
https://doi.org/10.1007/s13369-022-06585-z

RESEARCH ARTICLE-MECHANICAL ENGINEERING

Experimental Investigation and Molecular Dynamics Simulation of Contributing Variables on Abrasive Water Jet on Aluminum Alloy 7075 Reinforced with Al_2O_3, Graphite and Silicon Carbide

Bahman Parvandar Asadollahi[1] · Mohammad Pour Panah[2] · Akbar Javdani[3]

Received: 28 July 2021 / Accepted: 9 January 2022 / Published online: 5 February 2022

Abstract
The controversial issue in composite machining is usage of some nontraditional approaches to resolve the difficulty arising from composite machining. Thus, to obviate this difficulty, abrasive water jet machining could be applied. The purpose of this investigation is to study some responses such as material removal rate and kerf taper angle affected by some process parameters including traverse speed, water jet pressure, abrasive flow rate, various types of reinforcement particles, and their weight percentages via ANOVA analysis to evaluate their optimal level. Further, molecular dynamic simulations are applied to validate results obtained from experiments. For this purpose, the outcomes are described by temperature and potential energy of atomic to indicate the time for atomic equilibrium process and equilibrium phase of different simulated samples. In addition, to examine the effects of the process parameters, scanning electron microscopy and X-ray diffraction were used to determine the microstructure of machined surfaces and plastic deformation. The experimental results revealed that with reduction in the traverse speed (from 167.64 to 55.08 mm min^{-1}, weight percentage (7.5–2.5), water pressure (270–200 bar), and using SiC as reinforcement particle in matrix and an increase in flow rate (from 305 to 470 g min^{-1}), the kerf taper angle diminished, suggesting the high quality of machining. In this study, the results obtained from material removal rate and kerf taper angle showed that traverse speed is a substantial parameter in enhancing the quality of water jet machining.

Keywords Aluminum alloy 7075 · Aluminum oxide · Graphite · Abrasive water jet machining · Kerf taper angle · Molecular dynamics (MD) simulations

1 Introduction

To meet some specific needs in various applications comprising electronic instruments and military equipment, development of metal matrix composites (MMCs) has drawn plenty of attention to provide some unprecedented properties including enhanced modulus, specific stiffness, specific strength, wear, and corrosion resistance [1]. Abrasive waterjet machining (AWJM) is a promising method which could be applied for cutting processes. For the first time in 1980, for cutting material efficiently, abrasives were added to plain waterjet machines, which led to AWJM [2]. To machine heat-sensitive materials without significant effects on heat-affected zone (HAZ), AWJM is known as an advanced technology for varied machining [3]. In recent years, the production of ultrafine-grained (UFG)/nanostructured metal materials has gained extensive attention. This new generation of metal products has specific as well as higher physical and mechanical properties compared to coarse-grained materials. Since aluminum alloys with high and proper strength to weight ratio have various applications in the space industry, enhancing their mechanical properties is of great importance [4]. Delamination occurs from the abrasive penetration, leading to crack phenomenon in the case of composite material machining [5]. To overcome some problems arising from other machining techniques as well as to enhance the quality of machined surfaced, some water jet machining parameters including standoff distance, transverse distance, and

✉ Akbar Javdani
akbarjavdani@aut.ac.ir

[1] Mechanical Engineering Department, Faculty of Engineering, Shahid Chamran University of Ahvaz, Ahvaz, Iran

[2] Department of Physics, Faculty of Basic Sciences, Tarbiat Modares University, Tehran, Iran

[3] Non-Destructive Testing Lab, Department of Mechanical Engineering, Amirkabir University of Technology, Tehran, Iran

percentage tungsten carbide were optimized [6]. Shanmugasundaram [7] investigated the effects of water jet pressure and traverse rate as key factors on machined eutectic Ai–Si alloy/graphite composite surface to produce good finish surface. Karta et al. [8] carried out investigations to show the effects of AWJT machining process parameters on the average surface roughness, macro and micro surface characteristics. They found that nozzle feed rate, abrasive flow rate, and nozzle diameter affected average surface roughness significantly. In addition, the higher amount of material removal rate achieved in a single pass without any defects. Furthermore, an increase in flow rate surface roughness declined around 81%. However, surface roughness increased by 16% with an increase in nozzle feed rate. In addition to conventional experimental methods, computer simulations can also be used to predict the physical behavior of nanocomposites. Kartal [9] investigated the turning of AA5083 material by using abrasive water jet. He found that water jet turning process produced higher surface quality. Furthermore, during AWJM process larger amount of chip was removed without considerable defects. Moreover, He figured out that higher flow rate and turning speed improved the surface roughness. One of the most important simulations methods used to determine the mechanical behavior of atomic structures is the molecular dynamics (MD) approach [10, 11]. This computational method is employed to simulate various nanostructures such as Al-based nanocomposites. In previous works, Ward et al. [12] investigated the deformation and mechanism in Al–Si nanocomposites, formed by adding Si particles to Al nanocrystalline materials via MD simulations. They reported that the deformation and fracture mechanisms were different in the Al–Si composites as compared to single-phase Al structures. The plastic deformation of Al polycrystals is associated with a mix of grain boundary deformation and dislocation activity, while the deformation in the Al–Si nanostructures is associated with predominantly grain boundary sliding/shearing at the Al/Si interfaces and little deformation elsewhere. Elsewhere, Liu et al. [13] presented an atomistic study with MD approach on a chemical modification strategy, where the Al matrix was modified with Al_2O_3/Al_4C_3 nanoparticles to gain significantly improved interfacial shear strength and overall mechanical properties of graphene-reinforced aluminum (Al/Gr) nanocomposites. Furthermore, Patel et al. [14] explored the effect of various parameters such as length, diameter, and volume fraction of single wall carbon nanotube (SWCNT) on young's modulus and stress–strain behavior of SWCNT reinforced, Al matrix nanocomposite. MD simulations in this work revealed that young's modulus of SWCNT–Al nanocomposite was enhanced by 75.6 and 23.50% as compared to pure Al matrix by reinforcing 11.75 volume% of zig-zag (20, 0) and 8.81 volume% of armchair (10, 10) SWCNT in pristine structure, respectively.

The main purpose of this paper is to comprehensively survey the effects of some process parameters in AWJM machining including traverse speed, water jet pressure, and flow rate on hybrid aluminum matrix composite reinforced with various particles such as with different weight percentages via Taguchi method and ANOVA analysis. The significant novelty of this study is to investigate on the effects of abrasive water jet turning of hybrid aluminum matrix composite reinforced by various particles namely Al_2O_3, SiC, and graphite and implementing MD computational method to simulate the AWJM process on machined surfaces of samples for the worst and best cases. Through this method atom position and force-field defined in their structures are investigated. To validate these obtained results, scanning electron microscopy (SEM) and X-ray diffraction were applied to examine the surface characteristics of target material.

2 Experimental Procedure and Substances

2.1 Materials

In this investigation, 7075 aluminum alloy was used as the base metal. Table 1 reports the chemical composition of the material utilized in this investigation. Aluminum oxide, graphite, and silicon carbide powders were applied as reinforcement particles. Table 2 outlines the thermophysical properties of the mentioned materials. The alumina, graphite, and silicon carbide reinforcement particles sizes were 37, 45, and 40 ¯m, respectively. These reinforcement particles were added to the base metal in different weight percentages.

Figure 1 illustrates the morphology of the alumina, graphite, and silicon carbide as reinforcement particles, respectively.

2.2 Fabrication of Hybrid AMMC

In this study, aluminum metal matrix composites (Al 7075), as the matrix material, were applied in the preparation of

Table 1 Chemical composition of Al 7075

	Si	Fe	Cu	Mn	Mg	Cr	Zn	Ti	Others-each	Others-total	Al
Al 7075	0.40	0.50	1.2–2.0	0.30	2.1–2.9	0.18–0.28	5.1–6.1	0.20	0.05	0.15	Reminder

Table 2 Thermophysical properties of Al7075 alloy, C, Al_2O_3, and SiC

	Density (gm cm^{-3})	Thermal conductivity (W m^{-1})	Melting point (*c*)
Al7075	2.81	130	477–635
Al_2O_3	3.2	100	2072
SiC	55.885	24	3730
c	3.217	120	270

HMMCs. Steps stir casting process was undertaken for producing HMMCs. Stir casting setup included a furnace, reinforcement feeder, and mechanical stirrer, as displayed in Fig. 2. In this investigation, an electric resistance furnace was built. To make the vortex, mechanical stirrer was used leading to the mixing of reinforcement material. The impeller blade may be of diverse geometries and numbers of blades. In this research, flat blade with one number was chosen culminating in axial flow pattern. The mechanical stirrer was designed based on related Handbook [15]. To manufacture the mechanical stirrer from thin sheets, argon laser cutter was applied as shown in Fig. 3. Al7075 billets were kept in an electric crucible furnace and heated up to 750 °C for melting.

During the melting process, Al_2O_3, SiC, and graphite reinforcement particles with different weight percentages were first heated and then added to the base metal and heated up to 800 °C. To prevent discontinuity in the matrix composite microstructure, the temperature difference between matrix phase and reinforcement phase should be reduced. To improve wettability, argon gas was added to remove absorbed hydroxide and other gases. To mix the molten metal, Al_2O_3, SiC, and graphite reinforcement particles were stirred at 700 RPM for 15 min. Eventually, the composite melt was poured into mold to cool down. To enhance the quality of the composite sample made by stir casting technique, it was lathed as depicted in Fig. 4.

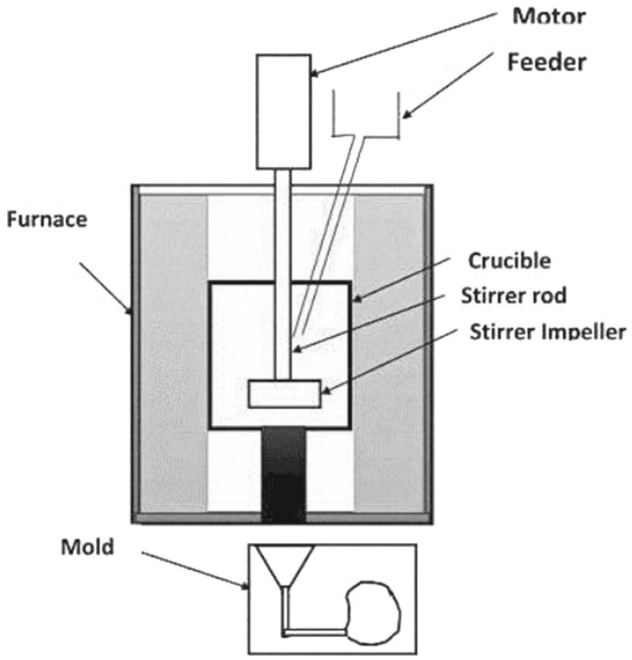

Fig. 2 Electric crucible furnace and its components [16]

2.3 Experimental Set Up (AAJ Machining)

The type of AAJ machining in this experiment has been shown in Fig. 5. In this investigation, one type of abrasive particles with #60 mesh size was applied. Water pressure (WP), traverse speed (TS), abrasive flow rate (AFR), and different reinforcement particles used in the matrix material or additive type (AT) as well as weight percentage of reinforcement (W%) were considered the main parameters for the machin-

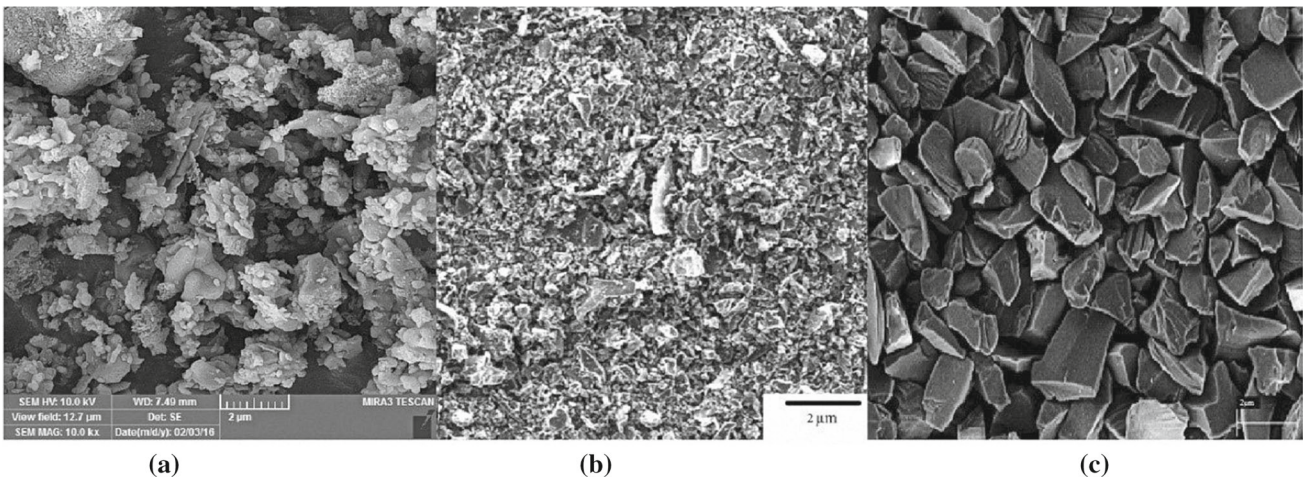

Fig. 1 SEM images of reinforcement particles. **a** Al_2O_3 particles with size of 37 ¯m, **b** graphite particles with size of 45 ¯m, and **c** SiC particles with size of 40 ¯m

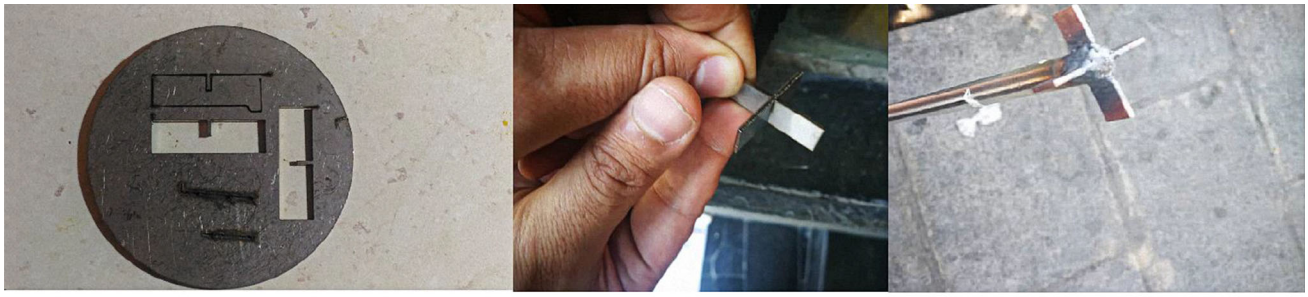

Fig. 3 The mechanical stirrer manufacturing process cutting with argon laser (**a**), inserting cut sheets (**b**), and welding sheets (**c**)

Fig. 4 Composite sample made by stir casting technique

Fig. 5 Abrasive water jet machine center

Table 3 Process and physical variables of abrasive water jet

Parameters	Range of operation
Impinging angle	90
Standoff distance	2 mm
Abrasive type	Garnet
Mesh size (MS)	60 mesh
Abrasive flow rate (AFR)	171, 305, 470 g min^{-1}
Water pressure (WP)	200, 240, 270 bar
Traverse speed (TS)	55.88, 99.06, 167.64 mm min^{-1}

ing process performed in the present study. These parameters and the range of operations are listed in Table 3.

2.4 Taguchi Method and Analysis of Variance (ANOVA)

The mentioned parameters and three distinct levels for each of them are presented in Table 4. Accordingly, many experiments should be conducted as cited above for full factorial design. To resolve this difficulty and reduce the number of required experiments, taguchi method was applied. In this method, a loss function is used to calculate variations between results and desired values. This function is referred to as "signal-to-noise ratio" [17], categorized into the lower-the-better, higher-the-better, and nominal-the-best [16]. To determine statically significant factors and reach the optimal combination of these factors, a statistical analysis of variance (ANOVA) is implemented. The purpose of this method in this investigation was to minimize the kerf taper angle and maximize the removal material rate. Hence, lower-the-better and higher-the-better were chosen for kerf taper angle and removal material rate, respectively, as outlined in Relations (1) and (2).

Lower-the-better (minimize):

$$\eta = \frac{s}{N_s} = -10\log\left[\frac{1}{n}\sum_{i=1}^{n} y_i^2\right] \tag{1}$$

Table 4 Factors and their levels

Parameters	Symbol	Level 1	Level 2	Level 3
Abrasive flow rate	AFR	171	305	470
Water pressure	WP	200	240	270
Traverse rate	TS	55.88	99.06	167.64
Additive type	AT	Al_2O_3	SiC	GRAPHITE
Weight percentage	V	55.88	99.06	167.64

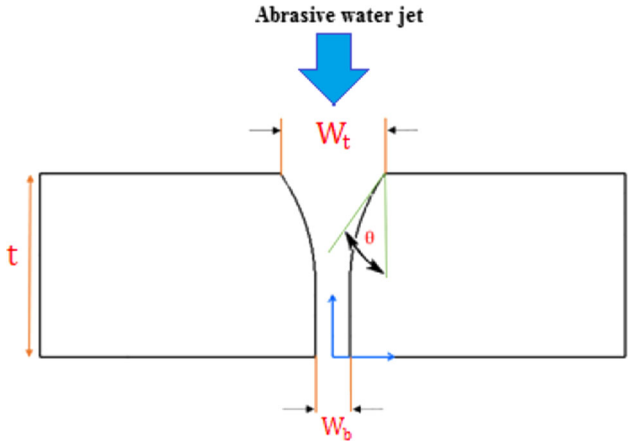

Fig. 6 Kerf taper geometry

Higher-the-better (maximize):

$$\eta = \frac{s}{N_s} = -10\log\left[\frac{1}{n}\sum_{i=1}^{n}\frac{1}{y_i^2}\right] \tag{2}$$

where y_i and n are obtained data and number of observed tests, respectively [18].

The geometry of the sample is a cylinder which has a diameter of 2 cm and a height of 2 cm. Output responses of this study are material removal rate and kerf taper angle.

2.5 Evaluation of Output Responses

Kerf taper angle was evaluated according to Relation (3), where θ is kerf taper angle (deg), and t denotes the thickness of work material (mm), as shown in Fig. 6 [9].

$$\tan\theta = \frac{\text{Top Kerf Width} - \text{Bottom Kerf Width}}{2t} \tag{3}$$

To measure the kerf taper angle, the sample was cut into four pieces, then two of them were glued together, as displayed in Fig. 7. Eventually, to measure the kerf taper angle, Optical Microscope Olympus BX51 was used. Figure 8 reveals the top and bottom kerf width taken 5 mm away from the sample. Accordingly, Fig. 8 reveals the kerf taper angle measurement and the quality of cutting.

MRR in this study was evaluated through measuring the weight of specimens before and after cutting with abrasive water jet. The amount of unwanted metal eroded from the measured sample has been expressed in Relation (4)[9].

$$\text{MRR} = \text{Depth of cut} \times \text{Traverse rate} \times \text{average kerf width} \left(\text{mm}^3/\text{min}\right) \tag{4}$$

3 Results and Discussion

3.1 Analysis of *S/N* Ratio and ANOVA Results

Table 5 presents the most appropriate orthogonal array of experimentation, which is L27. To better identify the experiments, symbols (*S*1…) have been assigned to them. In order to find the optimal process parameters, the signal-to-noise ratio (*S/N*) of each machining parameter level must be assessed for each output function. The minimum and maximum values of kerf taper angle and material removal rate, respectively, are values contributing to qualitative improvement of abrasive water jet. The mean values of material removal rate and kerf taper angle were 936.2694 (mm^3/min) and 0.41 (°), respectively. Similarly, the mean value of signal-to-noise ratio values for material removal rate and kerf taper were 57.62 (dB) and 18.88 (dB), respectively. The changes in material removal rate and kerf taper angle, which were obtained from the experimental investigation, are reported in Table 5.

T_{MRR} (Material removal rate total mean value) = 936.27 mm^3/min

$T_{\text{MRR-}S/N}$ (Material removal rate *S/N* ratio total mean value) = 57.63 dB

$T_{\text{Kerf taper angle}}$ (Kerf taper angle total mean value) = 0.41°

$T_{\text{Kerf taper angle }S/N}$ (Kerf taper angle *S/N* ratio total mean value) = 18.88 dB

Analysis of the effects of each control factor on material removal rate and kerf taper angle using *S/N* responses are shown in Table 6 based on the Taguchi technique. It indicates the optimal levels of control factors for the optimal material removal rate and kerf taper angle. The best level for each control factor was found based on the highest *S/N* ratio in the levels of that control factor. Indeed, higher amount of this ratio shows that the effect of uncontrollable factors (noise factor) is minimized. So, to reach the highest value for material removal rate, the controlling factors have been specified as follows: AFR (Level 3, *S/N* = 58.94), WP (Level 3, *S/N* = 58.26), TS (Level 3, *S/N* = 63.61), AT (Level 1, *S/N* = 59.51), and W% (Level 3, *S/N* = 59.06). Similarly, the

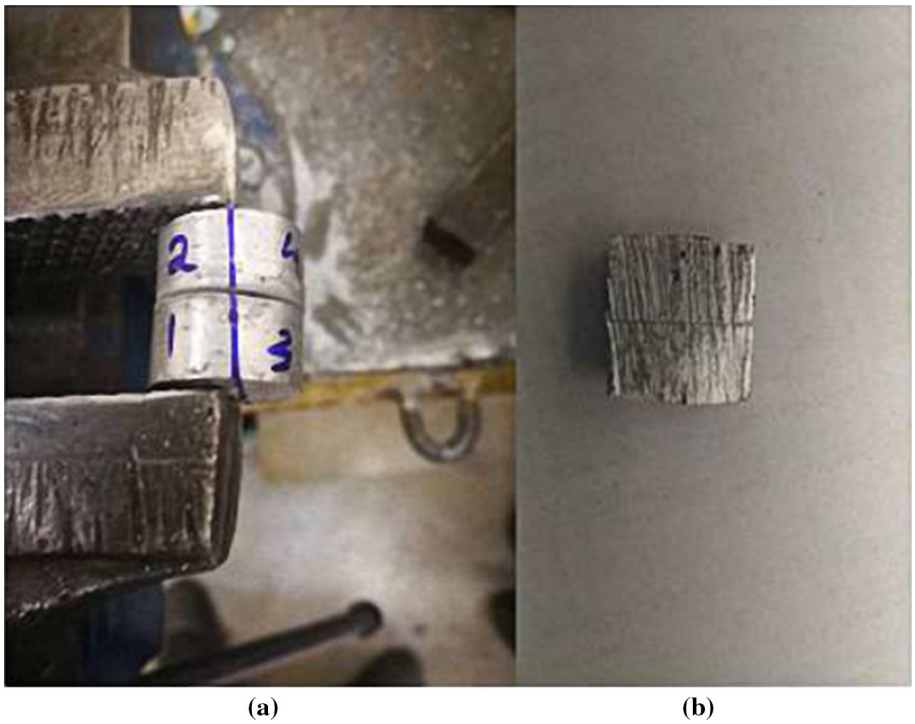

Fig. 7 The cylindrical sample cut into 4 pieces (**a**) and glued two cut pieces (**b**)

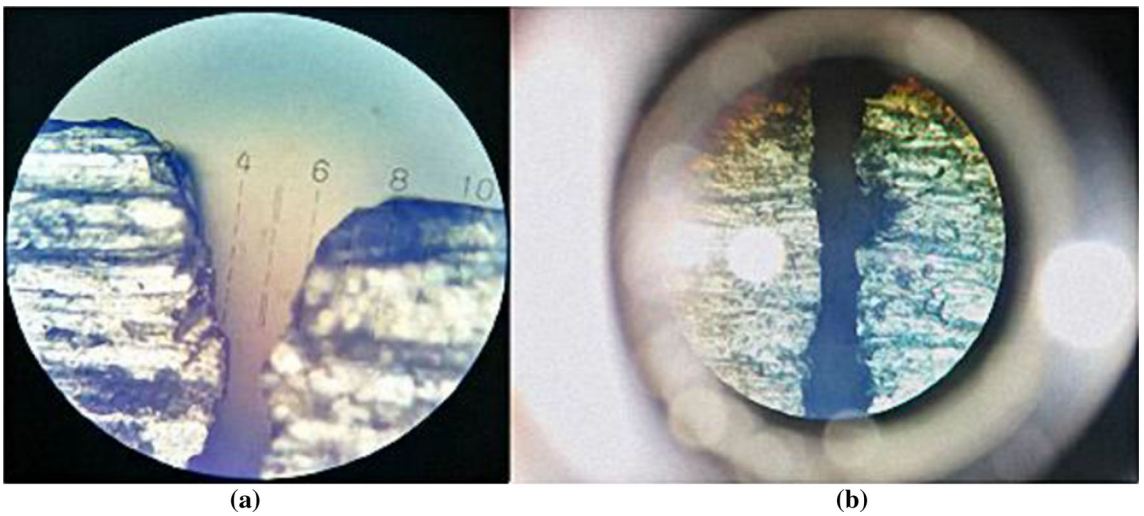

Fig. 8 Top kerf width (**a**) and bottom kerf width (**b**)

levels and *S/N* ratios for these parameters giving the best kerf taper angle were specified as AFR (Level 3, $S/N = 12.09$), WP (Level 1, $S/N = 11.23$), TS (Level 1, $S/N = 12.36$), AT (Level 2, $S/N = 13.32$), and W% (Level 1, $S/N = 12.57$).

Figures 9 and 10 depict the *S/N* ratio versus parameter level diagrams for kerf taper angle and material removal rate, respectively. Note that full cut occurred in all samples because of their small size. The percentage change in the weight of reinforcement particles has an important effect on the kerf taper angle. In other words, by changing the reinforcement particle weight percentage from 2.5 to 7.5%, kerf taper angle increases which reduces the quality of water jet cutting. This demonstrates that with an increase in the percentage of reinforcement particle in the matrix, the interaction between the reinforcement particles and the garnet particles (abrasive particles) grows and so does the composite hardness. Furthermore, the jet energy is reduced by reinforcement particles, thereby compromising the ability of jet energy for straight cut. Thus, it does not transfer powerful energy to matrix to penetrate into it straightly, culminating in higher kerf taper angle (Fig. 9f) and top kerf width, which elevates the material removal rate smoothly, as shown in Fig. 10f. Figure 9d indicates that with addition of silicon carbide as reinforcement particle to matrix, the kerf taper

Table 5 Influential variables of abrasive water jet process by taguchi method and the results of experiments and *S/N* ratio values

	AFR	WP	TS	AT	W%	Symbol	MRR ($mm^3\ min^{-1}$)	*S/N* ratio (dB) for MRR	Kerf taper (°) Angle	*S/N* ratio for Kerf (dB)
1	171	200	55.88	Al_2O_3	2.5	S1	599.59	55.56	0.18	14.80
2	171	200	55.88	Al_2O_3	5	S2	439.77	52.86	0.29	10.73
3	171	200	55.88	Al_2O_3	7.5	S3	301.75	49.59	0.34	9.29
4	171	240	99.06	SiC	2.5	S4	352.65	50.95	0.06	24.01
5	171	240	99.06	SiC	5	S5	209.07	46.40	0.20	14.02
6	171	240	99.06	SiC	7.5	S6	1174.85	61.40	0.88	1.12
7	171	270	167.64	Graphite	2.5	S7	932.08	59.39	0.63	99.06
8	171	270	167.64	Graphite	5	S8	1257.30	61.99	0.79	2.07
9	171	270	167.64	Graphite	7.5	S9	1332.74	62.49	0.56	4.95
10	305	200	99.06	Graphite	2.5	S10	495.30	53.90	0.43	7.34
11	305	200	99.06	Graphite	5	S11	526.01	54.42	0.47	6.48
12	305	200	99.06	Graphite	7.5	S12	1188.72	61.50	0.29	10.86
13	305	240	167.64	Al_2O_3	2.5	S13	1803.81	65.12	0.18	15.01
14	305	240	167.64	Al_2O_3	5	S14	1827.28	65.24	0.99	0.10
15	305	240	167.64	Al_2O_3	7.5	S15	1927.86	65.70	1.21	-1.65
16	305	270	55.88	SiC	2.5	S16	391.16	51.85	0.14	16.88
17	305	270	55.88	SiC	5	S17	449.83	53.06	0.10	19.38
18	305	270	55.88	SiC	7.5	S18	502.92	54.03	0.72	2.90
19	470	200	167.64	SiC	2.5	S19	1718.31	64.70	0.32	9.83
20	470	200	167.64	SiC	5	S20	2279.90	67.16	0.23	12.79
21	470	200	167.64	SiC	7.5	S21	1077.92	60.65	0.11	18.92
22	470	240	55.88	Graphite	2.5	S22	279.40	48.92	0.14	16.88
23	470	240	55.88	Graphite	5	S23	363.22	51.20	0.16	16.08
24	470	240	55.88	Graphite	7.5	S24	657.15	56.35	0.61	4.33
25	470	270	99.06	Al_2O_3	2.5	S25	1010.41	60.09	0.60	4.41
26	470	270	99.06	Al_2O_3	5	S26	1199.62	61.58	0.24	155.88
27	470	270	99.06	Al_2O_3	7.5	S27	980.69	59.83	0.21	13.35

Table 6 *S/N* response table for MRR and kerf taper angle

Levels	Control factors									
	Material removal rate (MRR)					Kerf taper Angle (Kerf)				
	AFR	WP	TS	AT	W%	AFR	WP	TS	AT	W%
Level 1	55.63	57.82	52.6	**59.51**	56.72	9.43	**11.23**	**12.36**	8.70	**12.57**
Level 2	58.31	56.81	51.64	56.69	57.10	8.58	9.99	10.42	**13.32**	10.43
Level 3	**58.94**	**58.26**	**63.61**	56.69	**59.06**	**12.09**	8.90	7.33	8.10	7.12
Delta	3.32	1.45	11	2.82	2.34	3.50	2.33	5.04	5.22	5.45
Rank	2	5	1	3	4	4	5	3	2	1

Highlight values demonstrate the optimal levels of control factors

angle diminishes, which can be attributed to the lowest hardness of silicon carbide compared to two other reinforcement particles. It means that the aqua jet breaks silicon carbide particles easily then transfer energy to the matrix, resulting in proper cut. In the composite with Al_2O_3 reinforcement particles, which has the highest hardness, the abrasive particles lost their energy and failed to cut in a straight direction after hitting reinforcement particles. In other terms, it produces a wide entrance for penetration, which leads to a higher material removal rate.

Figure 9c shows that the kerf taper angle has grown with the increase in water jet pressure. The higher water jet pressure generates greater kinetic energy of jet impinging onto workpiece, leading to the creation of a large kerf taper angle.

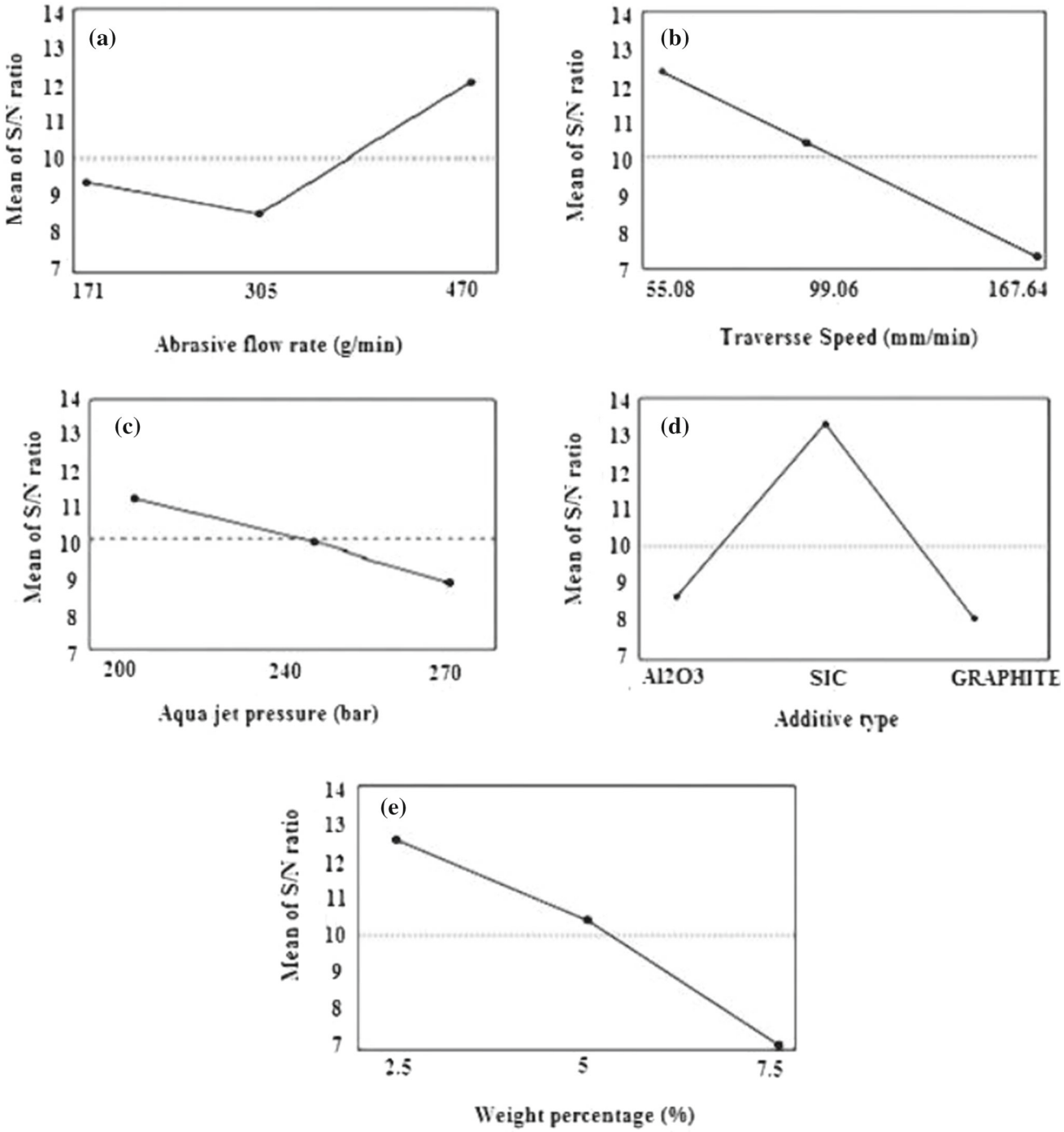

Fig. 9 *S/N* ratio analysis of kerf taper angle

However, it does not change the material removal rate significantly (Fig. 10c). The most predominant parameter in affecting the kerf taper angle and material removal rate is traverse speed, as displayed in Figs. 9b and 10b. The kerf taper angle has grown with the increase in traverse speed. As abrasive particles cannot mix with water properly because of the high speed of nozzle resulting in a poor machining at the bottom of the composite, then the kerf width is larger in the entrance and lower at the exit, which produces a larger kerf taper angle. In addition, the interaction of abrasive particles at the machined surface diminishes with the increase in traverse speed, which in turn, reduces the ability of jet to cut workpiece appropriately and straightly. Further, low traverse speed enhances the machining ability in the cutting surface, causing

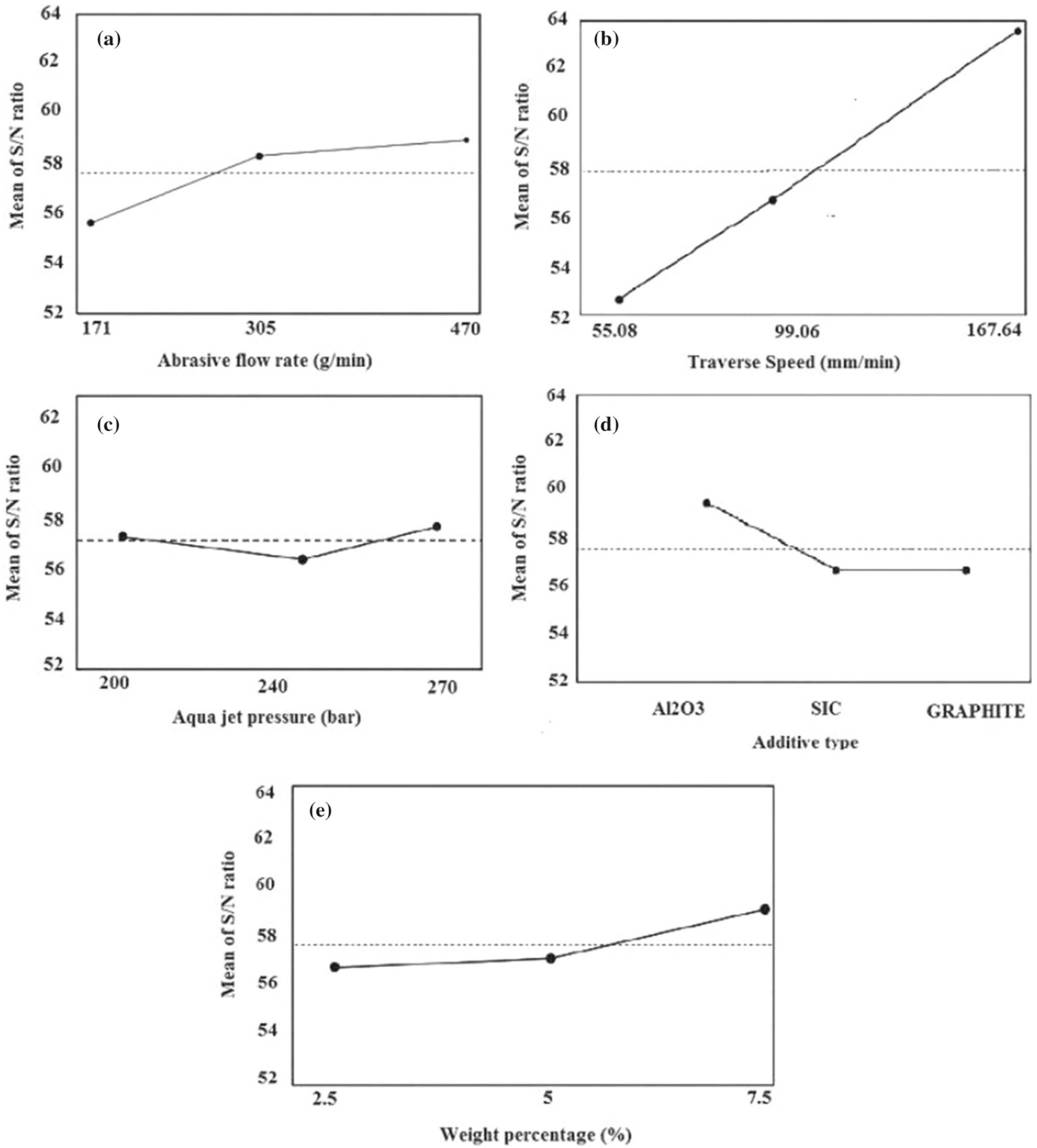

Fig. 10 *S/N* ratio analysis of material removal rate

generation of a small kerf taper angle. Abrasive flow rate has a key role in determining the cutting speed and machining time. It also pertains to the other process parameters including jet nozzle and jet speed [19]. Figure 9a reveals that the turning point of the curve is at the point with abrasive flow rate at 305 g min^{-1}. In this curve, the angle deviation of the kerf taper consistently dropped upon changing flow rate from 171 to 305 g min^{-1} and then started to grow with abrasive flow rate.

Figure 10b demonstrates that the traverse speed is directly proportional to material removal rate. It means that by elevating the value of traverse speed, material removal rate

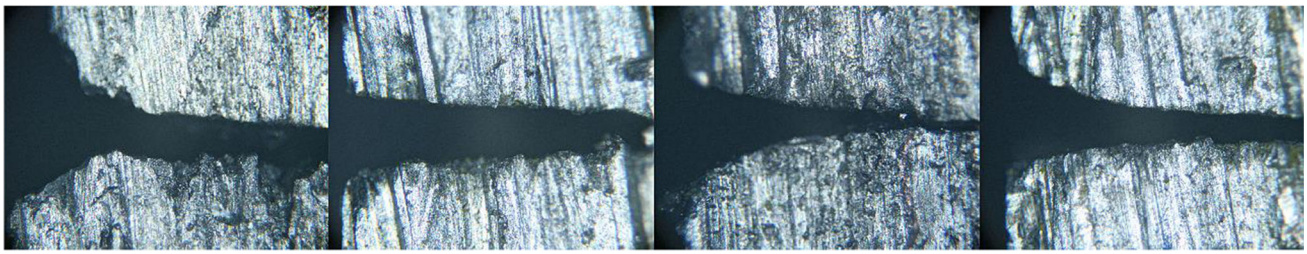

Fig. 11 Kerf width of S7, S1, S14, and S16 from left to right

Table 7 ANOVA analysis for material removal rate

Variance source	Degree of freedom	Sum of squares	Mean square	*F*-ratio	*P* value
MRR					
AFR	2	567,556	283,778	2.68	0.1
WP	2	22,833	11,417	0.11	0.9
TS	2	6,025,741	3,012,871	28.5	0
AT	2	531,953	265,976	2.51	0.11
W%	2	138,155	69,078	0.65	0.53
Error	16	1,692,343	105,771		
Total	26	8,978,582			

increases dramatically, i.e., at increased traverse speeds, MRR increases. On the other hand, upon enhancing the traverse speed, the deviation of jet increases which does not allow impressive interaction between water and abrasive particles, which is expected to reduce MRR. To explain this contradiction, by considering the fact that full cut happened in all samples, in this case the jet ability declines, causing reduced momentum transferred to the sample. Thus, it opens a wide entrance on the surface of sample for penetration, leading to a higher material removal rate. In other terms, the energy per unit area is inversely proportional to the traverse speed (this is clearly seen in laser cutting. It means that using powerful laser for cutting, a smaller opening is created on the surface of the sample, so the material removal rate in this condition decreases). At higher traverse speeds, reinforcement particles become unsteady, creating huge voids that can be seen on the surface of target sample, as shown in the SEM morphology section. At high abrasive flow rates, the interaction of garnet and reinforcement particles grows, culminating in dislodgement off the surface of the target sample. The number of abrasive particles per unit area of machined surface rises with an increase in abrasive flow rate, resulting in more removal of the target surface (Fig. 10a).

Figure 11 reveals the kerf taper angle for some samples. For its analysis, S7 and S16 samples were compared. Figure 11 shows that the kerf taper angle in S7 is larger than in S16. Based on Table 5, for S16 sample the contributing parameters were specified as traverse speed 55.88 mm/min^{-1} and SiC as reinforcement particle. However, for S7 sample, the important parameters included graphite as reinforcement particle and traverse speed 167.64 mm/min^{-1}. This suggests that with addition of graphite as reinforcement particle and an increase in traverse speed, the kerf taper angle grows significantly.

For meticulous evaluation, the contribution percentage of individual parameters to material removal rate and kerf taper angle was investigated through analysis of variance using Minitab software. The results obtained from ANOVA for material removal rate and kerf taper angle are presented in Tables 7 and 8. The effects of the above-mentioned control factors were examined through ANOVA which is a method to evaluate the efficiency of the mathematical models developed by RSM. The influence of various design factors and degree of sensitivity of the achieved outcomes toward the utilized factors that disturb the quality characteristics was specified. F-ratio value is a statistical equivalent to Taguchi's signal-to-noise ratio for the control factor effect versus the experimental error. This analysis was performed at a significance level of 5%, i.e., for a confidence level of 95%. Note that larger F-ratio represents that there is a significant modification on that control factor due to deviation of the process parameter. According to Table 7, larger F-ratio of transverse speed (28.5) indicates that it is a significant factor in material removal rate. Additionally, the *P*-values of traverse speed are lower than 0.001 value, suggesting that this control factor is heavily involved in material removal rate results, followed by flow rate, the type of reinforcement, weight percentage, and water pressure, respectively.

Based on the ANOVA results derived from Table 8, these parameters are not statistically significant. However, com-

Table 8 ANOVA analysis kerf taper angle

Variance source	Degree of freedom	Sum of squares	Mean square	*F*-ratio	*P* values
Kerf					
AFR	2	0.2102	0.10511	1.36	0.28
WP	2	0.1873	0.09366	1.22	0.32
TS	2	0.3204	0.1602	2.08	0.16
AT	2	0.1461	0.07306	0.95	0.41
W%	2	0.2867	0.14334	1.86	0.19
Error	16	1.2325	0.07703		
Total	26	2.3833			

Table 9 Atomic weight of various nanoparticles in under studied samples via MD approach

Sample ID (S)	SiC (%)	Al_2O_3(%)
S_4	2.5	–
S_5	5	–
S_{15}	–	7.5
S_{20}	5	–

pared to each other, traverse speed is relatively more effective [20]. Although low traverse speed allows more abrasives to strike the surface of sample, culminating in small kerf taper angle, it transfers lower kinetic energy due to low speed, which reduces the contribution of the traverse speed to affect kerf angle. The second effective control factor is flow rate; although at high flow rates, a large proportion of abrasive particles can cut the sample effectively they remove a larger width, which lessens the effect of high flow rate on kerf taper.

3.2 Molecular Dynamics Simulation

To validate the experimental method outputs, MD simulation results have been used in the current work. For this purpose, MD simulations were applied to simulate the AWJM process on four atomic samples for the best and worst cases which would produce the highest and lowest values in kerf angle (S_{15}, S_4) and material removal rate (S_{20}, S_5) (Table 9).

3.2.1 Computational Method

In the present research, atoms in Al 7075-based nanocomposite parts interact with each other for 12 ns. This atomic evolution defines their atomic stability and mechanical behavior. Technically, all MD simulations in this study were done by Large Scale Atomic Molecular Massively Simulator (LAMMPS) package [21]. Using this computational package, Al 7075-based nanocomposite was equilibrated at initial step for $t = 10$ ns whereby the AWJM process was implemented to the atomic structure for $t = 2$ ns. Computationally, the length of MD box in our computational phase was 100 Å along all directions. Furthermore, periodic boundary conditions were used in y and z directions, while the fixed one was implemented along x direction [22]. Figure 12 displays the initial atomic arrangement of Al 7075-based nanocomposite in the MD simulation box. After atomic modeling, force-field defining is necessary to estimate the atomic evolution of structures. For this purpose, universal force filed (UFF) and embedded atom model (EAM) can be used for simulated nanostructures [23]. In UFF force-field, the nonbond interaction between various atoms described by the Lennard–Jones (LJ) formalism is as follows [24]:

$$U(r) = 4\varepsilon\left[\left(\frac{\sigma}{r_{ij}}\right)^{12} - \left(\frac{\sigma}{r_{ij}}\right)^{6}\right] \quad r_{ij} \le r_c \tag{5}$$

In Eq. (5), epsilon constant is the depth of the potential well, sigma constant refers to the distance at which the potential is zero, and r_{ij} parameter is the distance between atoms with i and j IDs. The bonded interaction is another type of interatomic force in UFF force-field, defined by harmonic oscillator formalism for simple and angular interactions as the following equations [25]:

$$E_r = \frac{1}{2}k_r(r - r_0) \tag{6}$$

$$E_\theta = \frac{1}{2}k_\theta(\theta - \theta_0) \tag{7}$$

In Eqs. (6) and (7), $\frac{K_r}{K_\theta}$ and $\frac{r_0}{\theta_0}$ are the harmonic constant and equilibrium value of distance/angle in oscillator formalism, respectively. Furthermore, as mentioned earlier, EAM force-field used for atomic interaction defined in pristine Al matrix is as follows [25]:

$$E_i = F_\alpha\left(\sum_{i\neq j}\rho_\beta(r_{ij})\right) + \frac{1}{2}\sum_{j\neq i}\varphi_{\alpha\beta}(r_{ij}) \tag{8}$$

where F is the embedding energy. This computational parameter is a function of electron density for each atom (ρ), and φ is an atomic interaction parameter. Furthermore, α and β

labels are the element types of atoms i and j in MD box, respectively. Once the force-field is defined in the MD box, the Newton's second law is solved as the gradient of the defined force-field functions as the following equation [25].

$$F_i = \sum_{i \neq j} F_{ij} = m_i \frac{\mathrm{d}^2 r_i}{\mathrm{d}t^2} = m_i \frac{\mathrm{d}v_i}{\mathrm{d}t} = -\mathrm{grad}\ \mathrm{V_{ij}} \tag{9}$$

In the next step of MD simulations process, Nose–Hoover thermostat would be implemented to equilibrate of atomic structures at initial condition [26]. In this thermostat, the following equations can be used for "F" physical parameter calculation [26]:

$$f(N \cdot V \cdot T) = [N!\, Q(N \cdot V \cdot T)]^{-1} \int \mathrm{d}r^N \int \mathrm{d}p^N \exp\left[\frac{-H_1\left(r^N \cdot p^N \cdot V\right)}{KT}\right] F\left(r^N \cdot p^N \cdot V\right) \tag{10}$$

and,

$$Q(N \cdot V \cdot T) = (N!)^{-1} \int \mathrm{d}r^N \int \mathrm{d}p^N \exp\left[\frac{-H_1\left(r^N \cdot p^N \cdot V\right)}{KT}\right] \tag{11}$$

where N is number of atoms, V denotes volume of structure, H shows Hamiltonian, p represents atomic momentum, p is pressure, and K reflects the Boltzmann constant. Finally, the Velocity-Verlet approach was implemented regarding motion equations and time evolution of each atom in order to estimate the phase space calculations [27].

3.2.2 Results of MD Simulations

In the first step of this MD simulations, the equilibrium process of initial Al 7075-based nanocomposite was studied at $T_0 = 300$ K as initial temperature. The results obtained in this step show that the atomic position and force-fields defined in the simulated nanocomposite matched each other properly. This is described by temperature and potential energy of atomic nanocomposite calculation after $t = 10$ ns. As depicted in Fig. 13, the temperature of Al 7075-based nanocomposites converged to $T = 300$ K; this MD result shows that $t = 10$ ns is sufficient for atomic equilibrium detection. Furthermore, the potential energy calculation can show the equilibrium phase of various simulated samples. Numerically, the potential energy of samples 4, 5, 15, and 20 converted to – 6561 eV, – 6705 eV, – 7210 eV, and – 6993 eV, respectively, as presented in Fig. 14. From potential energy calculation, it is expected that the mechanical strength of sample 15 (S15) would have the maximum ratio among other atomic samples. Physically, the attraction force between atoms in the nanocomposite structure causes greater mechanical strength, which has been detected exactly in the next step of the current computational work.

Table 10 MRR and Kerf taper angle ratio of Al 7075-based nanocomposite after $t = 2$ ns

Sample	MRR ($mm^3\ min^{-1}$)	Kerf taper angle (°)
4	350.33	0.061
5	209.25	0.202
15	1924.46	1.235
20	2280.71	0.229

After equilibrium phase detection, the AWJM process was implemented in pristine nanocomposite as presented in Fig. 15. This figure shows the atomic evolution of Al-based nanocomposite in initial and final steps. As reported in the experimental section, the MRR and kerf taper angle reached the maximum ratio for samples 20 and 15, respectively. Furthermore, As outlined in Figs. 16 and 17, the MRR/kerf taper angle value has changed from 209.25 $mm^3\ min^{-1}$/0.061° to 2280.71 $mm^3\ min^{-1}$/1.235°; these results are in line with experimental results thus validating our initial method in this research (see Table 10).

4 Optimization of Responses

The aim of this investigation was to minimize the kerf taper angle and maximize MRR. The practical response values and corresponding process parameter values are depicted in Fig. 18. The point at which the red line intersects the response curve is considered as optimized values of the single process parameter. According to the obtained results seen in Fig. 18, AFR 470 g min^{-1}, WP 200 bar, TS 167.64 g min^{-1}, AT Al_2O_3, and W% 2.5% are optimized process parameters, which generate effective outcomes as MRR 2062.58 $mm^3\ min^{-1}$ and kerf taper angle 0.3306°. It also demonstrates that the composite desirability for optimized responses is 82.84%.

5 SEM Morphology

This section presents the SEM micrographs of the samples with larger and smaller kerf taper angle and material removal rate. It is proven that poor adhesion, pores or the formation

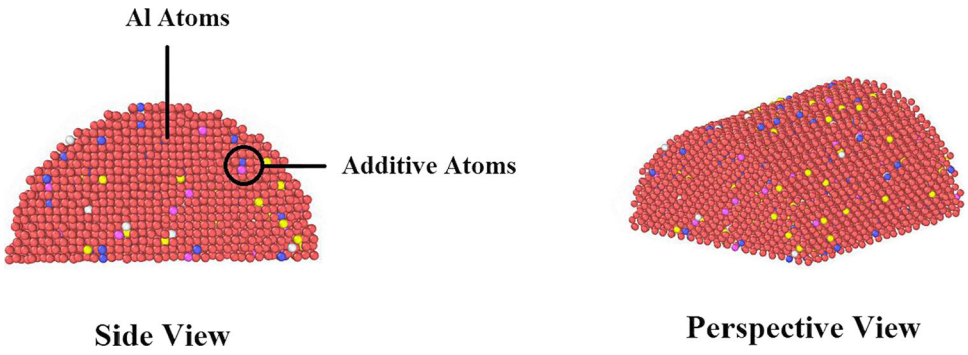

Fig. 12 Atomic representation of initial Al 7075-based nanocomposite simulated with LAMMPS package

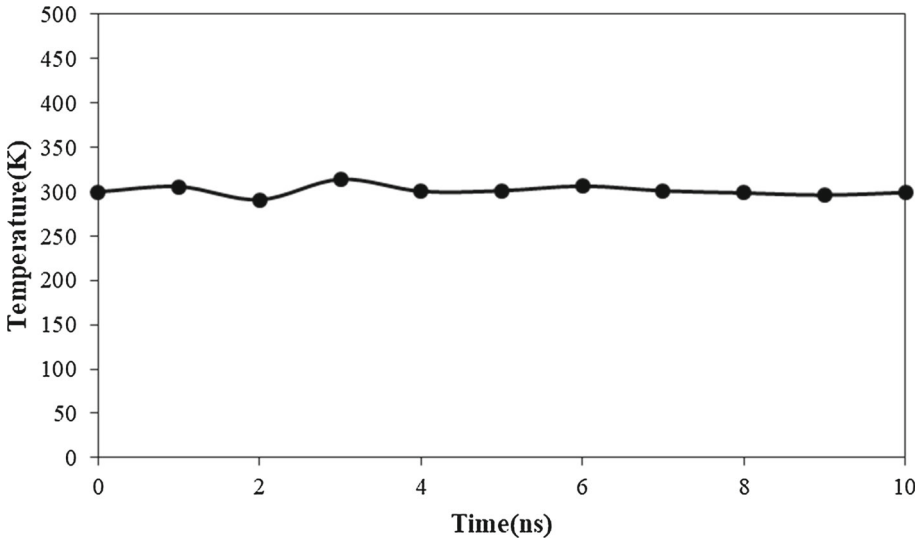

Fig. 13 Temperature changes of Al 7075-based nanocomposite as a function of MD simulation time

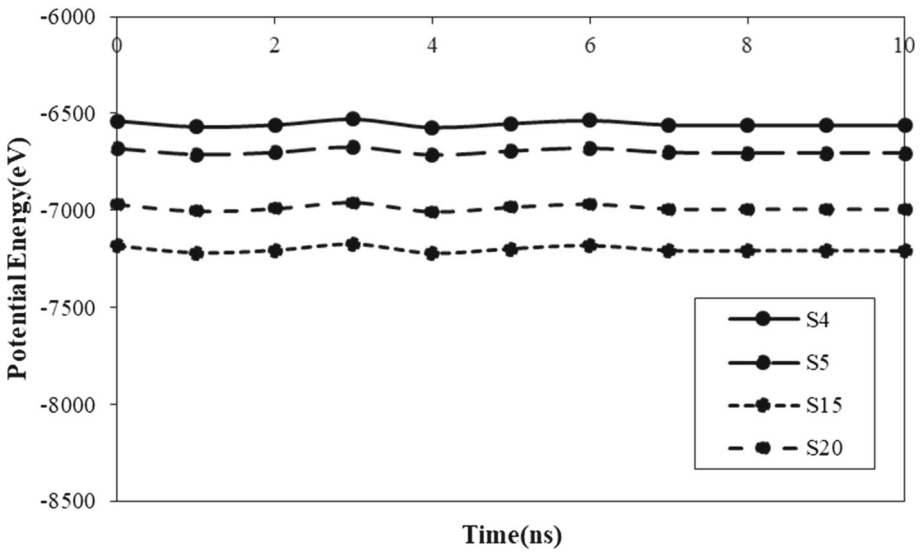

Fig. 14 Potential energy changes of Al 7075-based nanocomposite (various samples) as a function of MD simulation time

of brittle intermetallic phases at the interface between matrix and reinforcements may result in premature and catastrophic failure of the composites. This analysis was carried out on the cut surfaces with diverse magnifications such as 150×, 1 K, 5 K, 10 K, and 15 K. SEM images indicate the cutting performance of abrasive particles rubbing against the material surface and leaving wear tracks with random directions. In Fig. 19, the delamination phenomenon can be seen at the cut surface, which is the consequence of damage to the cut surface and crack growth. S15 sample with Al_2O_3 reinforcement particles with the weight percentage of 7.5% subjected to AWJ cutting with traverse speed of 167.64 mm min^{-1} pro-

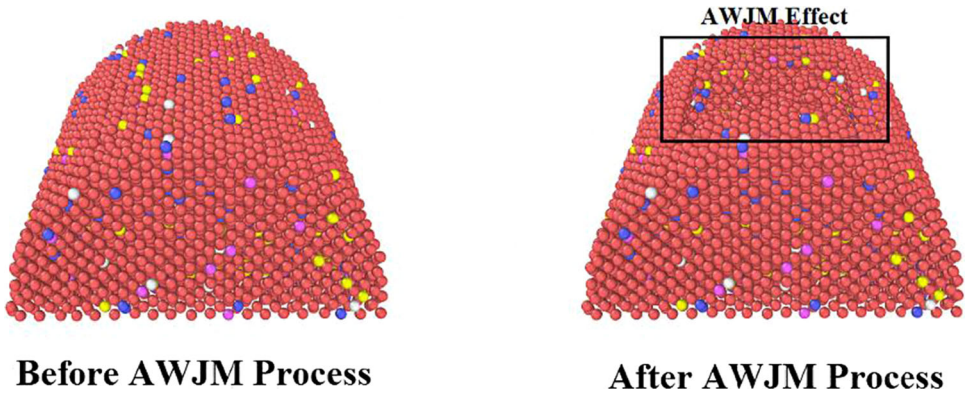

Fig. 15 The atomic arrangement of MD simulated matrix before and after of AWJM process

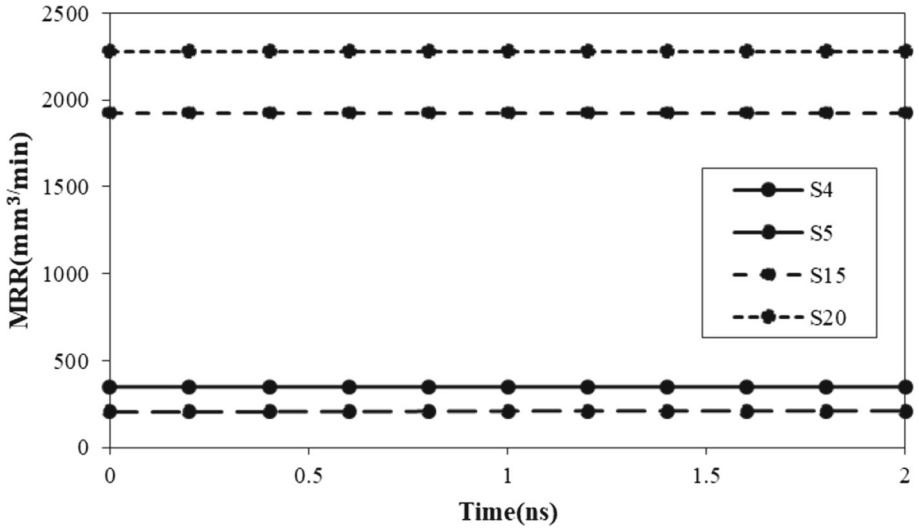

Fig. 16 MRR changes of Al 7075-based nanocomposite (various samples) as a function of MD simulation time

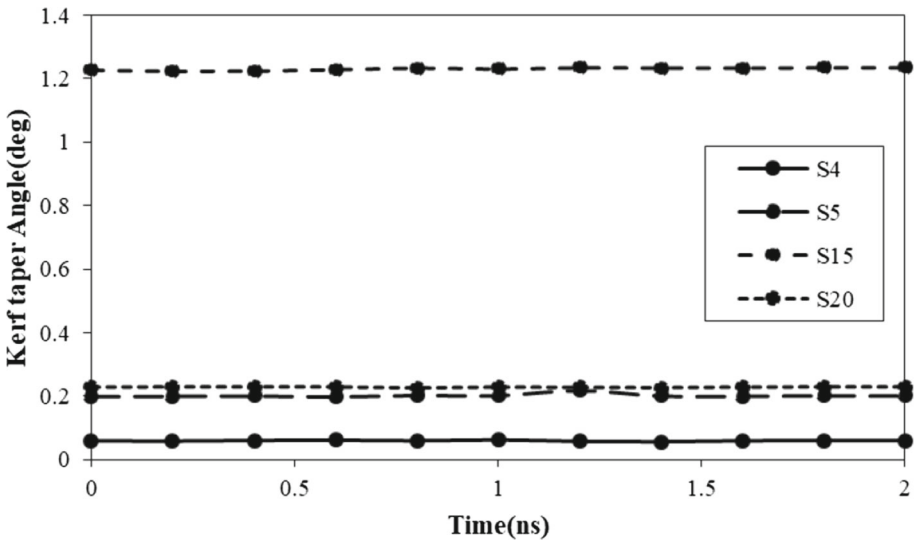

Fig. 17 Kerf taper angle changes of Al 7075-based nanocomposite (various samples) as a function of MD simulation time

duced a larger kerf taper angle compared to S4 sample. The higher weight percentage of reinforcement particles in S15 sample is clearly seen in Fig. 20 in the form of cluster. The presence of microcracks indicates that the samples are brittle in nature. Erosion of particle reinforcements at higher traverse speed causes voids at the surface, affecting the quality of machining.

Plowing phenomenon can be seen in Fig. 20, which was the result of erosive mechanism owing to plastic deformation surrounded by an intense impingement. Deep and long trajec-

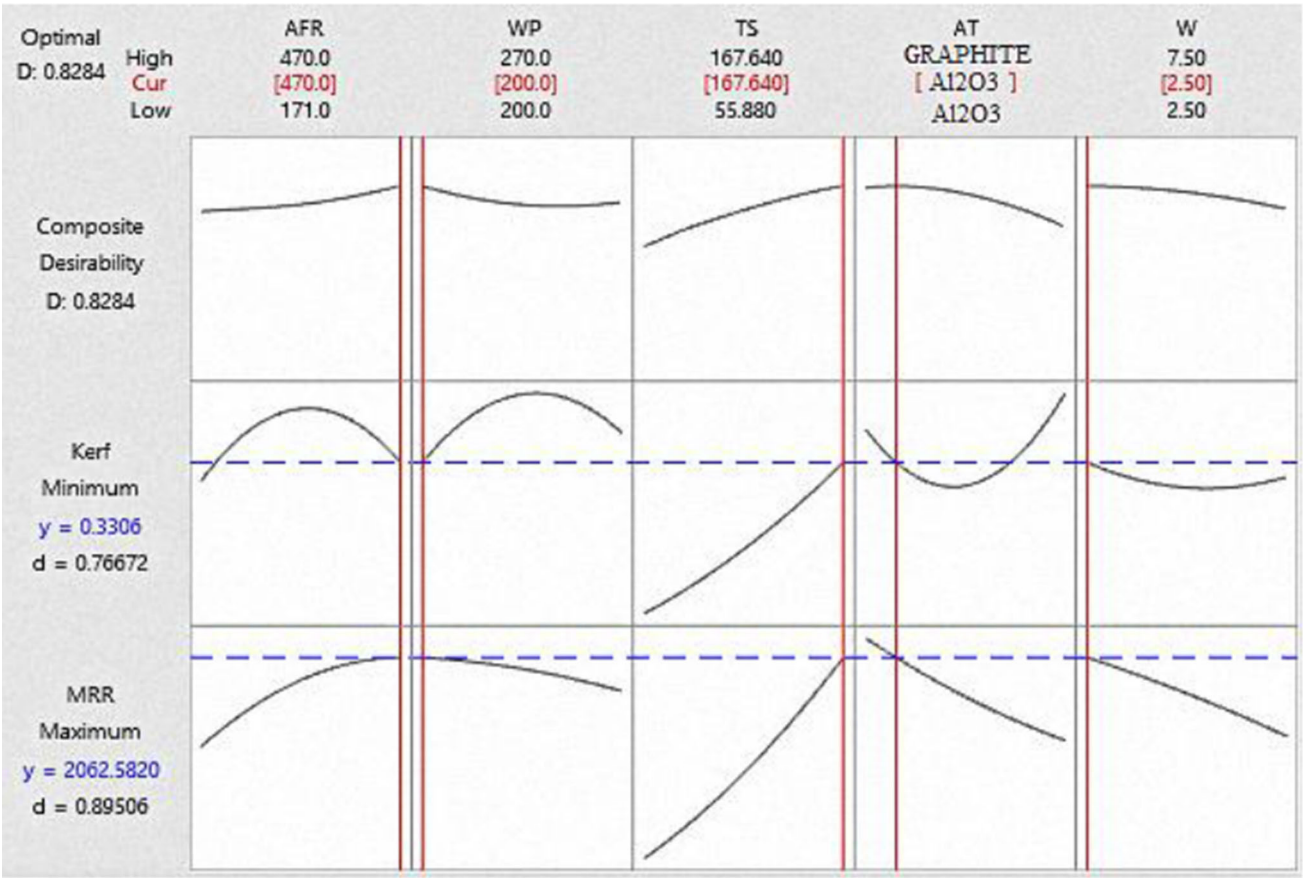

Fig. 18 Composite desirability for optimized responses in AWJ process

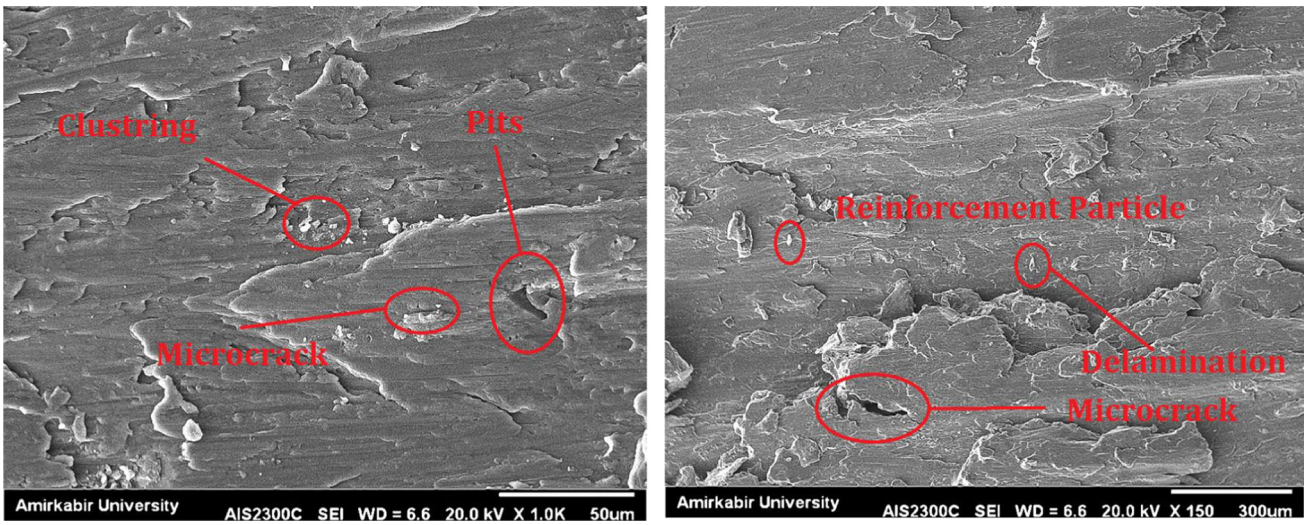

Fig. 19 SEM images of cut surface for S4 sample (minimum kerf taper angle)

tories were seen in S15 (which has higher material removal rate compared to S4), resulting in higher abrasive flow rate and traverse speed, which would increase the level of interaction between garnet particles and reinforcement particles. In addition, this increase causes reinforcement particles to obtain the threshold energy and detach from the sample, leading to void formation.

SEM images of the cut surface for S20 and S5 samples are shown in Figs. 21 and 22, respectively. The delamination phenomenon can be observed in both cut surfaces in these

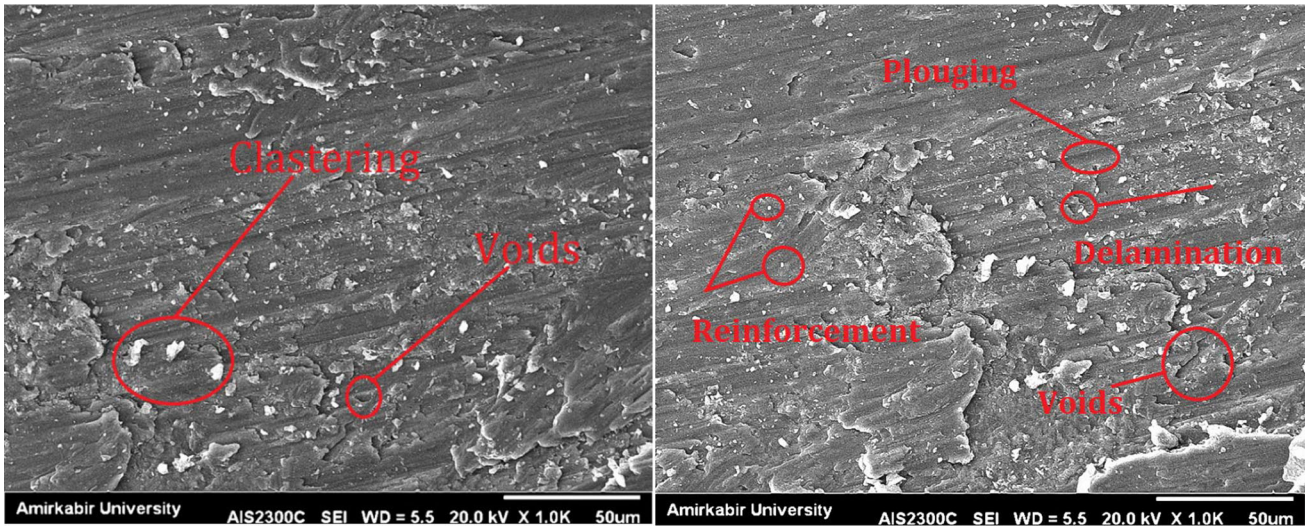

Fig. 20 SEM images of cut surface for S15 sample (maximum kerf taper angle)

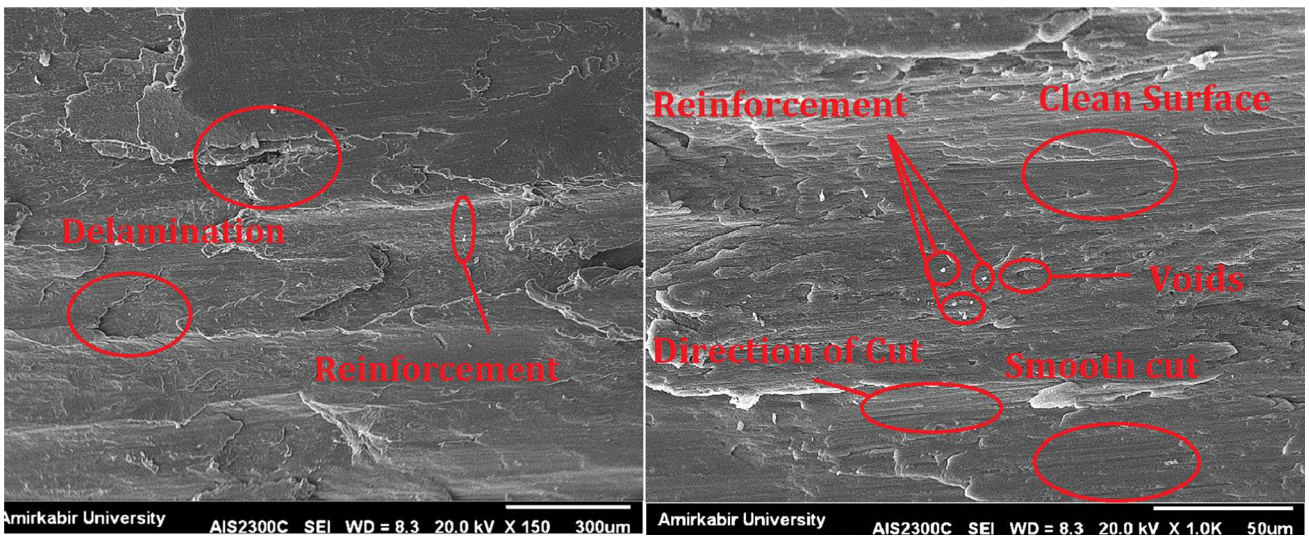

Fig. 21 SEM images of cut surface for S20 sample (maximum MRR)

two figures. Nevertheless, it is far more severe in Fig. 22, demonstrating poor cut mechanism for S5 sample subjected to the lowest material removal rate. Figure 21 indicates that high abrasive flow rate gave rise to more abrasive particles involved in the cutting mechanism through removing the grooved line, which was produced during the cutting wear mechanism. Hence, it removed a large amount of material, which produced a smooth surface.

Furthermore, some surface defects such as voids and craters that have been detected are considered insignificant in comparison to larger removal of material during the cutting process. Damages are seen in Fig. 22 in the form of microcracks. Under low erosion force arising from low abrasive flow rate, the erosion process became weaker which eventuated in the surface not being polished properly. Further, intensive plastic deformation is shown in Fig. 22. In all SEM images, there are no entrapped garnet particles which is because of high momentum of the garnet particles and the small thickness of the work specimen.

6 XRD Analysis

Figure 23 indicates the XRD pattern of bulk samples with Al_2O_3, SiC and graphite reinforcement particles, respectively. There is a large difference in the relative peak intensity between the sample depicted Fig. 23a, and two other samples displayed in Fig. 23b, c, indicating higher strength of Al_2O_3 reinforcement particles compared to SiC and graphite. Figure 23b reveals the XRD pattern of bulk sample with

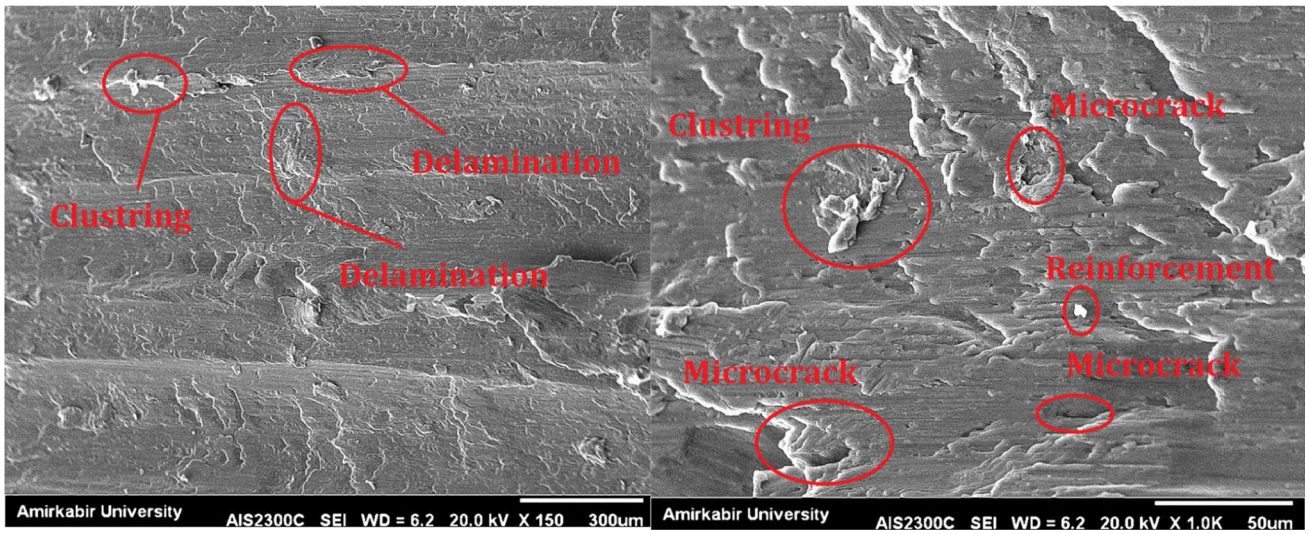

Fig. 22 SEM images of cut surface for S5 sample (minimum MRR)

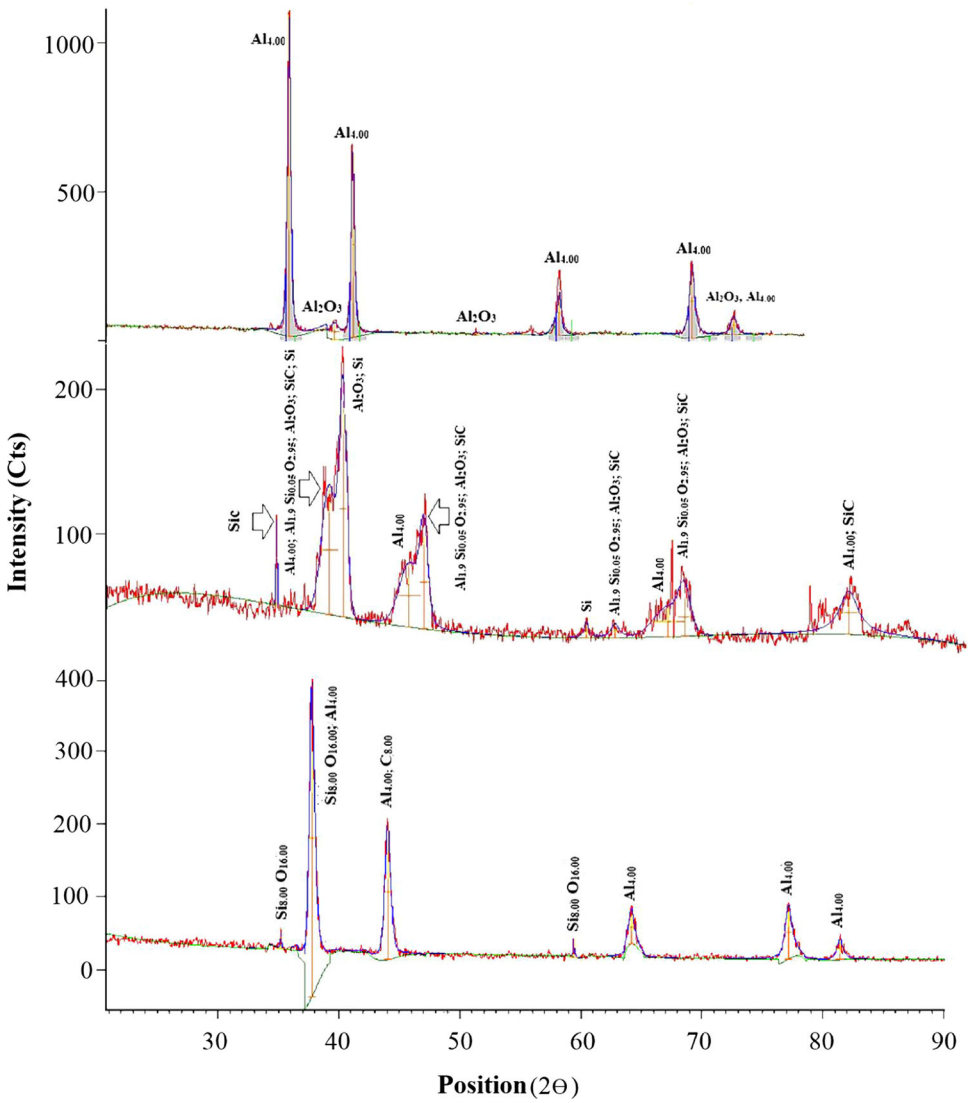

Fig. 23 XRD pattern of bulk samples with Al_2O_3 (**a**), SiC (**b**) and graphite reinforcement particles (**c**)

SiC reinforcement particles. It is observed in Fig. 23b that the simulated patterns for SiC exhibits broader and weaker peaks compared to the sample with Al_2O_3 reinforcement particles. In addition, it consists of different phases leading to peak broadening due to overlapping peaks. This broadening may have resulted from the reaction of aluminum and silicon phases (note that some silicon content is available in aluminum alloy illustrating high reactivity of silicon with aluminum). In other words, some of the silicon elements are separated from the silicon carbide and reacted with aluminum, creating new phases resulting from these compounds such as aluminum silicate, leading to reduced peak intensity.

The XRD pattern of the bulk sample with graphite reinforcement particles is depicted in Fig. 23c. The broadening of the XRD peaks is partially observed. In addition, the peak intensity of bulk sample with graphite reinforcement is lower compared to the sample with Al_2O_3 reinforcement particles. The key point in Fig. 23c is peak shifting in XRD toward lower angle side owing to solubility of carbon within the aluminum structure (carbon in its free form does not blend with aluminum at low ratios), which reduces the peak intensity of the bulk sample with graphite reinforcement particles. The significant point deduced from XRD images is the higher strength of the bulk sample with Al_2O_3 reinforcement particles in comparison to other samples.

7 Conclusion

A study of AWJ cutting of hybrid aluminum alloy matrix reinforced with Al_2O_3, SiC, and graphite using stir casting method was carried out to investigate cutting quality characteristics based on some process parameters including traverse speed, abrasive flow rate, water pressure, type of reinforcement particles, and their weigh percentage.

1. The L_{27} Taguchi orthogonal design of experiments was conducted, and cutting operation of samples was done to investigate the effects of process parameters on some responses such as material removal rate and kerf taper angle.
2. According to the ANOVA results, the most dominant parameter, affecting the quality of cutting, was traverse speed. With an increase in traverse speed, the kerf taper angle increased, which is caused by poor mixing of abrasive particle and water jet producing larger width which demonstrates the low quality of cutting operation. However, it elevated the material removal rate dramatically due to high energy transferred to the surface of the sample. Furthermore, high traverse speed left voids at the cut surface and created microcracks.
3. Higher abrasive flow rate provides excellent interaction between the abrasive particles and reinforcement particles culminating in a high material removal rate and low kerf taper angle. In other terms, the higher proportion of abrasive particles are allowed to strike the sample surface. A large number of abrasive particles produce a smooth surface. Shown in Fig. 21.
4. To achieve a small kerf taper angle, the weight percentage of reinforcement particles should be minimum, which would reduce the surface hardness of the composite.
5. SEM micrographs revealed the existence of particle contamination, groves, microcracks, and delamination in the cut surface. Also, the XRD pattern of bulk samples confirmed strength differences in shown particle reinforced composites in response to the presence of different reinforcement particles.
6. Achieved results in molecular dynamics simulation reveal that the atomic position and force-fields matched each other accurately.

Authors' Contribution Bahman Parvandar Asadolahi: Designed the analysis, Performed and wrote the analysis. Mohammad Pour Panah: Designed the analysis, Akbar Javdani: Designed the analysis, Proof reading.

Declarations

Conflict of interest The authors declare that they have no conflicts of interest.

Availability of Data and Materials Data available on request from the authors.

Code Availability LAMMPS and Minitab 20.02.0.0 main inputs available on request from the authors.

References

1. Ramanathan, A.; Krishnan, P.K.; Muraliraja, R.: A review on the production of metal matrix composites through stir casting: furnace design, properties, challenges, and research opportunities. J. Manuf. Processes **42**, 213–245 (2019). https://doi.org/10.1016/j.jmapro.2019.04.017
2. Gupta, K. Introduction to Abrasive Water Jet Machining. In: Abrasive Water Jet Machining of Engineering Materials; Springer: Berlin/Heidelberg, Germany, 2020; pp. 1–11.
3. Liu, X.; Liang, Z.; Wen, G.; Yuan, X.: Waterjet machining and research developments: a review. Int. J. Adv. Manuf. Technol. **102**, 1257–1335 (2019)
4. Javdani, A.; Pouyafar, V.; Ameli, A.; Alex, A.: Volinsky, blended powder semisolid forming of Al7075/Al_2O_3 composites: investigation of microstructure and mechanical properties. Mater. Des. **109**, 57–67 (2016)
5. Ruiz-Garcia, R.; Ares, P.F.M.; Vazquez-Martinez, J.M.; Gomez, J.S.: Influence of abrasive waterjet parameters on the cutting and drilling of CFRP/UNS A97075 and UNS A97075/CFRP stacks. Materials **12**, 107 (2019)

6. Kumar, K.R.; Sreebalaji, V.S.; Pridhar, T.: Characterization and optimization of Abrasive Water Jet Machining parameters of aluminum/tungsten carbide composites. Measurement **117**, 57–66 (2018)
7. Shanmughasundaram, P.: Influence of abrasive water jet machining parameters on the surface roughness of eutectic Al–Si alloy—graphite composites. Mater. Phys. Mech. **19**(1), 1–8 (2014)
8. Kartal, F.; Yerlikaya, Z.: Effects of machining parameters on surface roughness and macro surface characteristics when the machining of Al-6082 T6 alloy using AWJT. Measurement (2016). https://doi.org/10.1016/j.measurement.2016.10.007
9. Kartal, F.: Study and evaluation of abrasive water jet turning process performance on AA5083. Mater. Sci. Eng. Technol. (2020). https://doi.org/10.1002/mawe.201900099
10. Alder, B.J.; Wainwright, T.E.: Studies in molecular dynamics. I. General method. J. Chem. Phys. **31**(2), 459–466 (1959). https://doi.org/10.1063/1.1730376
11. Rahman, A.: Correlations in the motion of atoms in liquid argon. Phys. Rev. **136**(2A), A405–A411 (1964). https://doi.org/10.1103/PhysRev.136.A405
12. Ward, D.K.; Curtin, W.A.; Qi, Y.: Mechanical behavior of aluminum–silicon nanocomposites: a molecular dynamics study. Acta Mater. **54**(17), 4441–4451 (2006). https://doi.org/10.1016/j.actamat.2006.05.022
13. Liu, J., et al.: Mechanical properties of graphene-reinforced aluminum composite with modified substrate surface: a molecular dynamics study. Nanotechnology **32**, 085712 (2021)
14. Patel, P.R.; Sharma, S.; Tiwari, S.K.: Molecular dynamics simulation of single-wall carbon nanotube aluminum composite. In: Saha, S.K.; Mukherjee, M. (Eds.) Recent advances in computational mechanics and simulations. Lecture notes in mechanical engineering, Springer (2021)
15. Mixing of Solid–Liquid System, Process Engineering Guide: GBHE-PEG-MIX-703.
16. Gupta, A.; Singh, H.; Aggarwal, A.: Taguchi-fuzzy multi output optimization (MOO) in high-speed CNC turning of AISI P-20 tool steel. Expert Syst. Appl. **38**, 6822–6828 (2011)
17. Asilturk, I.; Akkus, H.: Determining the effect of cutting parameters on surface roughness in hard turning using the Taguchi method. Measurement **44**, 1697–1704 (2011)
18. Mandal, N.; Doloi, B.; Mondal, B.; Das, R.: Optimization of flank wear using Zirconia Toughened Alumina (ZTA) cutting tool: taguchi method and regression analysis. Measurement **44**, 2149–2155 (2011)
19. Parikh, P.J.; Lam, S.S.: Parameter estimation for abrasive water jet machining process using neural networks. Int. J. Adv. Manuf. Technol. **40**(5–6), 497–502 (2009)
20. Ramin, M.; Ghader, F.; Akbar, J.; Vahid, P.: Combined effects of ECAP and subsequent heating parameters on semi-solid microstructure of 7075 aluminum alloy. Trans. Nonferrous Met. Soc. China **26**, 3091–3101 (2016)
21. Brown, W.M.; Kohlmeyer, A.; Plimpton, S.J.; Tharrington, A.N.: Implementing molecular dynamics on hybrid high performance computers: particle–particle particle-mesh. Comput. Phys. Commun. **183**(3), 449–459 (2012). https://doi.org/10.1016/j.cpc.2011.10.012
22. Mai, W.; Li, P.; Bao, H.; Li, X.; Jiang, L.; Hu, J.; Werner, D.H.: Prism-based DGTD with a simplified periodic boundary condition to analyze FSS with D2n symmetry in a rectangular array under normal incidence. IEEE Antennas Wirel. Propag. Lett. **18**(4), 771–775 (2019). https://doi.org/10.1109/LAWP.2019.2902340.ISSN1536-1225
23. Rappe, A.K.; Casewit, C.J.; Colwell, K.S.; Goddard, W.A.; Skiff, W.M.: UFF, a full periodic table force field for molecular mechanics and molecular dynamics simulations. J. Am. Chem. Soc. **114**(25), 10024–10035 (1992). https://doi.org/10.1021/ja00051a040
24. Lennard-Jones, J.E.: Cohesion. Proc. Phys. Soc. **43**(5), 461–482 (1931)
25. Rapaport, D.C.: The Art of Molecular Dynamics Simulation. Cambridge University Press, Cambridge (1996)
26. Nosé, S.: A unified formulation of the constant temperature molecular-dynamics methods. J. Chem Phys. **81**(1), 511–519 (1984). https://doi.org/10.1063/1.447334
27. Press, W.H.; Teukolsky, S.A.; Vetterling, W.T.; Flannery, B.P.: Section 17.4. Second-Order Conservative Equations: Numerical Recipes: The Art of Scientific Computing, 3rd edn. Cambridge University Press, New York (2007)